Advanced Model for Predicting Buckling in Rails

David H. Allen
Professor
Director, Center for Railway Research
Ocean Engineering Department
Texas A&M University/Texas A&M Transportation Institute

Ting-Ming Liu
Ph.D. Student
Ocean Engineering Department
Texas A&M University/Texas A&M Transportation Institute

A Report on Research Sponsored by

University Transportation Center for Railway Safety (UTCRS)

Texas A&M University (TAMU)

September 30, 2025

Technical Report Documentation Page

<table>
<tr><td colspan="2">1. Report No.
UTCRS-TAMU-I1CY24</td><td>2. Government Accession No.</td><td colspan="2">3. Recipient's Catalog No.</td></tr>
<tr><td colspan="3" rowspan="2">4. Title and Subtitle

Advanced Model for Predicting Buckling in Rails</td><td colspan="2">5. Report Date
September 30, 2025</td></tr>
<tr><td colspan="2">6. Performing Organization Code
UTCRS-TAMU</td></tr>
<tr><td colspan="3">7. Author(s)
D.H. Allen and T.-M. Liu</td><td colspan="2">8. Performing Organization Report No.
CRR-2025-02</td></tr>
<tr><td colspan="3" rowspan="2">9. Performing Organization Name and Address
University Transportation Center for Railway Safety (UTCRS)
Center for Railway Research (CRR)
Texas A&M University (TAMU)
College Station, TX 77843</td><td colspan="2">10. Work Unit No. (TRAIS)</td></tr>
<tr><td colspan="2">11. Contract or Grant No.
69A3552348340</td></tr>
<tr><td colspan="3" rowspan="2">12. Sponsoring Agency Name and Address
U.S. Department of Transportation (USDOT)
University Transportation Centers Program
1200 New Jersey Ave. SE
Washington, DC, 20590</td><td colspan="2">13. Type of Report and Period Covered
Project Report
June 1, 2024 – August 31, 2025</td></tr>
<tr><td colspan="2">14. Sponsoring Agency Code
USDOT UTC Program</td></tr>
<tr><td colspan="5">15. Supplementary Notes
Collaborative project with MxV Rail (Rail Industry Research Testing Facility)</td></tr>
<tr><td colspan="5">16. Abstract
It is well-known that track buckling is one of the most commonplace causes of train derailments. Accordingly, with funding provided by the USDOT UTC program and the Technology Transportation Center, Inc., we have now completed developing a Beta-version track buckling model for deployment by U.S. Railroad Companies as a tool for predicting track buckling. This new generation of our buckling model utilizes a displacement incrementation formulation that provides the ability to predict the post-buckled response of rails. Note that this is a significant advancement over currently deployed track buckling models. Furthermore, our track buckling model accounts for the effects of the following on track buckling: both longitudinal and lateral track walk; rail neutral temperature (RNT); both lateral and longitudinal nonlinear crosstie aggregate interfacial friction; track modulus; nonlinear track liftoff; and broken spikes. In addition, it is sufficiently robust to be capable of accounting for additional environmental causes, and we are working together with MxV Rail on a regular basis to supply predictions of these effects for their use and potential supply to the U.S. Rail Industry. Given these advanced capabilities, it is anticipated that track engineers will be able to dramatically mitigate track failures due to buckling. The results provided herein are from a paper currently in submission for publication in a refereed journal.</td></tr>
<tr><td colspan="2">17. Key Words
Buckling, Construction and Maintenance, Computer Models</td><td colspan="3">18. Distribution Statement
This report is available for download from
https://www.utrgv.edu/railwaysafety/research/infrastructure/index.htm</td></tr>
<tr><td>19. Security Classification (of this report)
None</td><td colspan="2">20. Security Classification (of this page)
None</td><td>21. No. of Pages
35</td><td>22. Price</td></tr>
</table>

Table of Contents

List of Figures

List of Tables

List of Abbreviations

CWR	Continuous Welded Rail
FRA	Federal Railroad Administration
NTSB	National Transportation Safety Board
STPT	Single-Tie Push Tests

Disclaimer

Acknowledgments

The authors want to acknowledge the University Transportation Center for Railway Safety (UTCRS) for the financial support provided to perform this study through the USDOT UTC Program under Grant No. 69A3552348340. We also acknowledge the input provided to this research by Dr. Stephen Wilk, research scientist at MxV Rail, Pueblo, CO.

A Finite Element Framework for Rail Buckling Using Displacement Control

T. Liu, V. Musu, D. H. Allen, S. Wilk

Abstract

Rail buckling is a nonlinear instability problem influenced by multiple service conditions, including train passage, thermal stress, track misalignment, tie-ballast interaction, and complex boundary effects. To address the challenge of modeling this phenomenon efficiently while preserving physical fidelity, this study presents a finite element model based on Euler-Bernoulli beam theory, implemented in Python. The framework is designed to be computationally lightweight, with individual simulations completing within minutes, making it suitable for parametric studies and engineering applications.

The model builds upon prior foundational studies by incorporating a displacement-controlled solution algorithm, which offers numerical advantages over traditional force-control approaches, particularly in capturing post-buckling behavior. This capability is critical for assessing structural response when unexpected energy input—such as train effects—pushes the system beyond critical thresholds. To further enhance model realism, a nonlinear tie-ballast resistance formulation is introduced, calibrated to replicate responses observed in single-tie push tests (STPT).

Results demonstrate that displacement control enables robust and accurate simulation, and that the model reliably captures the influence of initial misalignments and the nonlinearity of the lateral resistance. The findings underscore the utility of displacement control not only in improving numerical convergence but also in providing meaningful insight into failure mechanisms under various track conditions.

Rail Structures, Buckling, Finite Element Method, Displacement Control, Euler-Bernoulli Beam Theory, Geometrical Nonlinearity, Single-Tie Push Test

1. Introduction

Rail buckling poses a serious threat to railway safety and infrastructure reliability, with recent data indicating that approximately 11% of train accidents between 2021 and 2023 may be attributed to buckling-related failures (Federal Railroad Administration, 2024). These incidents can result in costly disruptions and, in some cases, human casualties. Despite growing attention in recent years, there remains a lack of practical, deployable modeling tools for predicting and preventing buckling failures under varying field conditions.

Figure 1: Photograph showing thermally induced buckling of a railway (reprinted with permission from ABproTWE, CC BY-SA 3.0, via Wikimedia Commons)

Buckling in continuous welded rail (CWR) systems is primarily induced by thermal stresses, often happening during hot weather conditions, commonly referred to as "sun kinks," as observed in events such as the 2002 Amtrak derailments in Florida and Maryland (National Transportation Safety Board, 2003, 2004). However, it is also strongly influenced by multiple secondary factors, including geometric imperfections, crosstie/ballast degradation, train-induced lift-off, and boundary constraints. Field observations and post-incident analyses consistently show that initial misalignments and weak tie-ballast resistance zones play a pivotal role in triggering these failures.

Theoretical modeling of rail behavior under thermal loading traces back to classical beam theory, with Euler's work on beam deformation (1744) forming the foundation for later railway-specific applications by Timoshenko (1915, 1927) and others. The concept of modeling rails as beams on elastic foundations has been progressively refined over the decades. Notably, the formulations by Kerr (1974, 1976) and subsequent finite element implementations by Tvergaard and Needleman (1981) introduced nonlinear lateral resistance models and demonstrated that imperfections can drastically reduce critical buckling temperatures, leading to localized post-buckled configurations. Recent work by Yang and Bradford (2016) emphasized the importance of displacement-controlled solution schemes to accurately capture unstable post-buckling behavior, where force-controlled algorithms often fail.

Specifically, Tvergaard and Needleman (1981) employed a Rayleigh-Ritz technique to predict global buckling of elastic structures, providing efficient solutions but limited in their applicability to track systems with localized nonlinearities. Yang (2016) presented a comprehensive framework for thermally induced rail buckling and post-buckling behavior,

initially solving a linearized eigenvalue problem to determine the critical buckling load and subsequently applying single and multiple shooting methods to trace post-buckling equilibrium paths under prescribed displacements.

While these approaches advanced the theoretical understanding of rail instability, they present limitations for field applications. Rayleigh-Ritz methods typically assume smooth, global deformation modes and are not readily adaptable to systems with discrete tie supports, nonlinear ballast resistance, or localized fastener stiffness without significant modification of the assumed displacement fields. Shooting methods, though capable of capturing post-buckling behavior, require reformulating the boundary value problem into a sequence of initial value problems during numerical integration, are sensitive to initial guess accuracy, and often demand domain segmentation to maintain numerical stability under large deformations. Moreover, many prior formulations assume simplified ballast resistance models that do not fully capture the progressive reduction of track support observed under large displacements.

Commercial finite element software is increasingly applied to model CWR buckling (e.g., Pucillo, 2016; Miri et al., 2021). Despite their capabilities, these tools often involve long runtime, high licensing costs, and steep learning curves, making them overly complex for direct application by field engineers.

To address these challenges, this work presents a finite element-based displacement-control framework for rail buckling simulation. Building upon the methodology of Musu (2023), the model incorporates a displacement-control algorithm adapted from the self-correcting displacement incrementation method introduced by Haisler, Stricklin, and Key (1977). Developed in Python and based on Euler-Bernoulli beam theory, the model also includes nonlinear resistance functions calibrated to STPT data, updated variational formulations, and flexible input parameters such as tie spacing, rail profile, and ballast friction coefficients. It captures key nonlinearities—such as tie-ballast interaction, local track parameter variations, track lift-off, large strain effects, and geometric nonlinearities—while maintaining minimal computational cost.

Unlike previous displacement-control schemes, the proposed model stably follows equilibrium paths into the post-buckling regime by directly solving the full nonlinear coupled system. Additionally, the displacement control point can be assigned to any nodal degree of freedom, including both displacements and rotations, offering full flexibility to simulate realistic boundary conditions, misalignments, or external disturbances. A parametric study is conducted to assess the effects of lateral tie-ballast resistance, and the simulation results show that the lateral resistance is a crucial factor for rail buckling, agreeing with established experimental and theoretical trends (e.g., Li & Batra, 2007; Kish & Samavedam, 2013). With runtime measured in minutes on a standard Intel Core i7 laptop, the developed tool offers a practical and field-ready simulation capability for engineers and researchers focused on rail stability analysis and preventive maintenance planning.

A preliminary version of this model and its underlying framework appears in the first author's doctoral dissertation (Liu, 2025), where additional derivation details and extended case studies are provided.

2. Model Development

This section summarizes the key assumptions used in model development. For the full derivation and additional details, see Liu (2025).

2.1. Overview of The Track Structure

As illustrated in Figure 2, the track is affixed to the crossties using fasteners (spikes). The ballast, composed of crushed stone aggregate, is deposited on the rail bed beneath the ties, which are typically embedded within it. Note that the coordinate axes x, y, and z correspond to the axial, lateral, and vertical directions relative to the direction of travel.

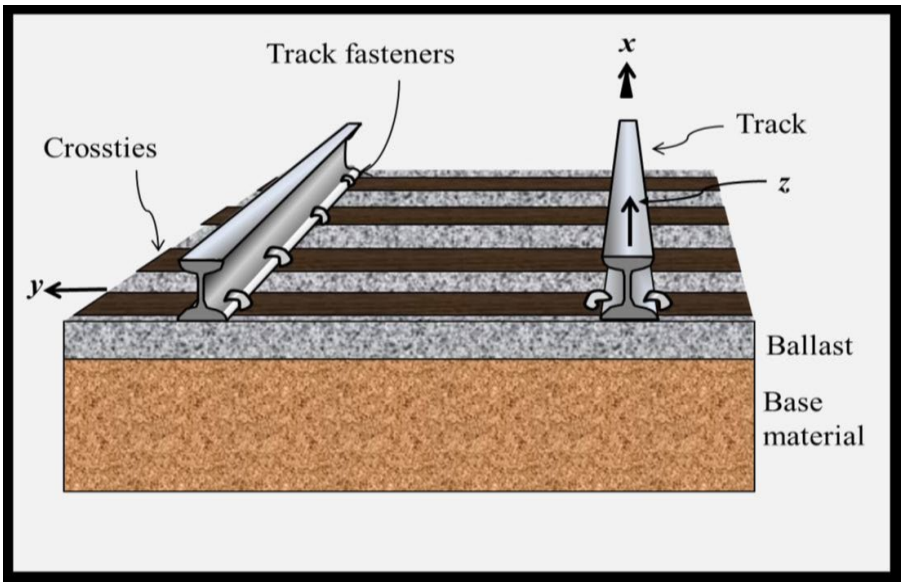

Figure 2: Generic rail with right-handed coordinate system as shown (reprinted with Permission from Allen and Fry, 2017)

2.2. Effects on the Track

In this study, five primary effects are considered in the mechanical model: lateral tie–ballast resistance, longitudinal tie–ballast resistance, vertical support from the ballast, rotational restraint provided by the rail fasteners, and thermally induced axial stresses. Incorporating these effects is essential for accurately capturing the mechanical behavior of the track and for formulating a well-posed boundary value problem suitable for numerical analysis.

The ties fastened to the track provide resistance that helps limit track deformation. Studies indicate that the tie-ballast interaction contributes additional resistance and behaves in a strongly nonlinear manner (Samavedam et al., 1995).

For lateral tie-ballast resistance (F_y), this research has deployed the results of single-tie push tests (STPT) (Wilk, 2024). STPTs are experiments that apply a lateral load to a single tie embedded within the track structure to measure the force-displacement relationship, as depicted in Figure 3.

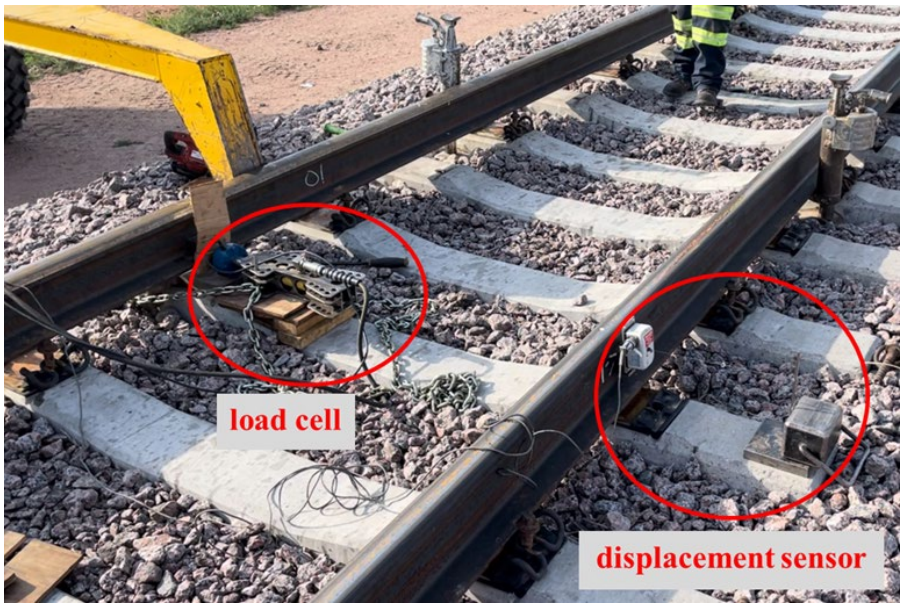

Figure 3: Photograph showing the Operation of a Single-Tie Push Test Experiment Conducted by MxV Rail, Pueblo, CO (reprinted with Permission from Liu, 2025)

Although the tie is disconnected from the original track during the experiment, it is still embedded in the ballast, implying that the resistance measured is caused strictly by tie-ballast interaction. Thus, in the remainder of this research, the term lateral resistance refers specifically to the lateral tie–ballast resistance, unless otherwise stated. The lateral resistance is modeled using a generalized trilinear force–displacement relationship that captures two key physical states of the track system: the disturbed and compacted conditions. These conditions represent different levels of ballast consolidation, typically governed by maintenance history and traffic-induced compaction.

In the compacted condition, the ballast has undergone sufficient consolidation through repeated train loading, resulting in well-interlocked aggregates and a higher peak lateral resistance. The force–displacement behavior in this case is characterized by an initial linear increase in resistance with displacement, reaching a peak value ($F_{y,pk}$), followed by a gradual decrease in force until it stabilizes at a residual limit value ($F_{y,lt}$). In contrast, the disturbed condition, which typically occurs after tamping operations, features a loose ballast structure with lower resistance. This behavior can be represented as a special case of the trilinear model in which the peak and limit resistances are equal, effectively reducing the curve to a bilinear form. This unification allows a single mathematical formulation to represent both physical states by adjusting the peak and limit parameters accordingly.

The mathematical expressions for this generalized resistance function are provided in Equation (1), where $F_{y,pk}$, $F_{y,lt}$, v_{pk}, and v_{lt} define the key parameters of the relation. A sign function is applied to ensure that the lateral resistance opposes the direction of displacement. Figure 4 shows representative STPT experimental results along with curve-fitted trilinear models, illustrating the flexibility of the formulation to fit both compacted and disturbed conditions.

$$F_y(v) = \begin{cases} \dfrac{F_{y,pk}}{v_{pk}} \cdot |v| \cdot \mathrm{sgn}(-v), & |v| \le v_{pk} \\ \left[F_{y,pk} + \dfrac{F_{y,lt} - F_{y,pk}}{v_{lt} - v_{pk}} \cdot \left(|v| - v_{pk}\right)\right] \cdot \mathrm{sgn}(-v), & v_{pk} < |v| \le v_{lt} \\ F_{y,lt} \cdot \mathrm{sgn}(-v), & |v| > v_{lt} \end{cases} \quad (1)$$

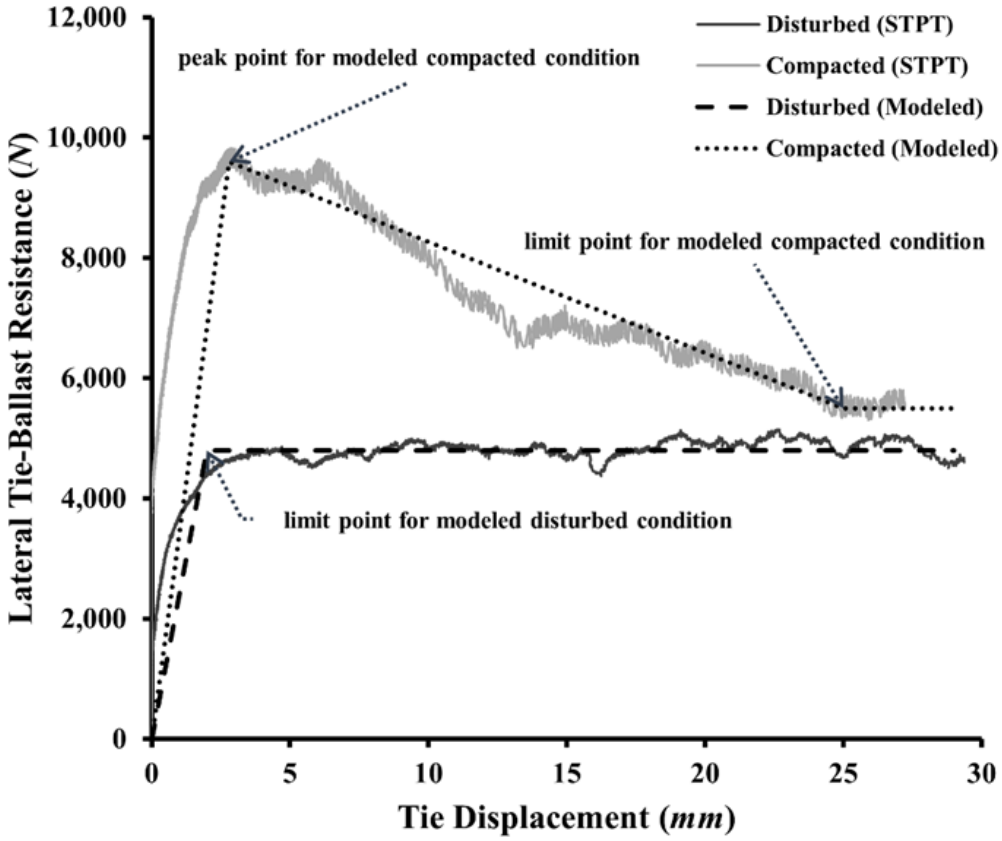

Figure 4: Demonstration of actual STPT experiment results alongside the corresponding curve-fitting model for the displacement-resistance relationship (reprinted with Permission from Liu, 2025)

A similar approach is applied to the longitudinal tie-ballast resistance (F_x), which varies with axial displacement (u). Although previous studies have suggested that this relationship is inherently nonlinear (Tvergaard and Needleman, 1981; Nobakht et al., 2022), the precise governing mechanism remains unclear and needs to be further investigated. As a practical simplification, F_x is assumed to vary linearly with u in this study, as shown in Equation (2):

$$F_x(u) = -k_x \cdot u \quad (2)$$

Here, k_x is the longitudinal stiffness and is assumed to be constant. The term longitudinal resistance is used similarly to denote the longitudinal tie–ballast resistance, following the same assumptions and modeling approach as the lateral case.

Before these resistance models are incorporated into the finite element formulation, additional calibrations are performed. The lateral resistance comprises three main components (Li et al., 1997): friction beneath the tie, friction along the tie sides, and shoulder resistance from the surrounding ballast, as shown in Figure 5. A similar breakdown applies to longitudinal resistance.

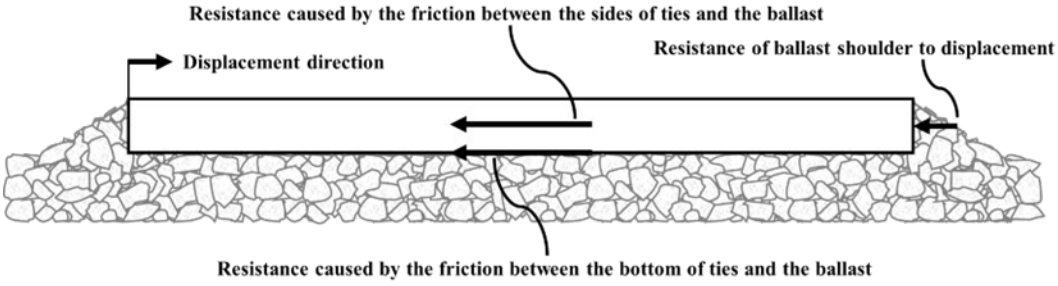

Figure 5: Illustration of the tie-ballast interaction, showing the three major lateral resistance components (reprinted with Permission from Liu, 2025)

To generalize the STPT-derived resistance curves to different tie weights, loading conditions, and tie–ballast interface properties, a scaling factor (λ_i) is introduced using Coulomb's friction law:

$$\lambda_i = \frac{F_i + \mu \cdot N - \mu_{STPT} \cdot N_{STPT}}{F_i} \tag{3}$$

Here, subscripts i denote the corresponding direction (longitudinal or lateral), and subscripts STPT represent the values specific to the STPT experiments. This factor accounts for differences in vertical load (N) and friction coefficient (μ) between the experiment and the modeled track section and should be multiplied to the curve fit Equations (1) and (2) to capture these effects. It is important to note that in this model, vertical load is assumed to affect only the bottom friction component, while the side and shoulder contributions remain unchanged.

Finally, the lumped resistance forces F_x and F_y are converted into distributed loads f_x and f_y by dividing by the tie spacing (d_{tie}). These distributed terms (Equations (4) and (5)) are then used as inputs along the rail in the finite element model to represent tie–ballast interaction throughout the track.

$$f_x(u) = \frac{\lambda_x \cdot F_x}{d_{tie}} \tag{4}$$

$$f_y(v) = \frac{\lambda_y \cdot F_y}{d_{tie}} \tag{5}$$

In contrast to the x and y axes—where frictional effects are considered—friction in the z direction is taken to be negligible. Even so, the ballast supplies vertical support that is idealized as springs, so the vertical reaction force (f_z) is assumed to vary linearly with the vertical displacement (w), according to:

$$f_z(w) = -k_z \cdot w \tag{6}$$

Here, f_z is already described as distributed loads and has units of force per unit length. The track modulus (k_z) is assumed to be a constant and can be acquired from experimental data (Oden, 1967).

In addition to the forces in the x, y, and z direction, fasteners are used to connect tracks and ties and can provide rotational resistance to prevent the rail from bending, as shown in Figure 6:

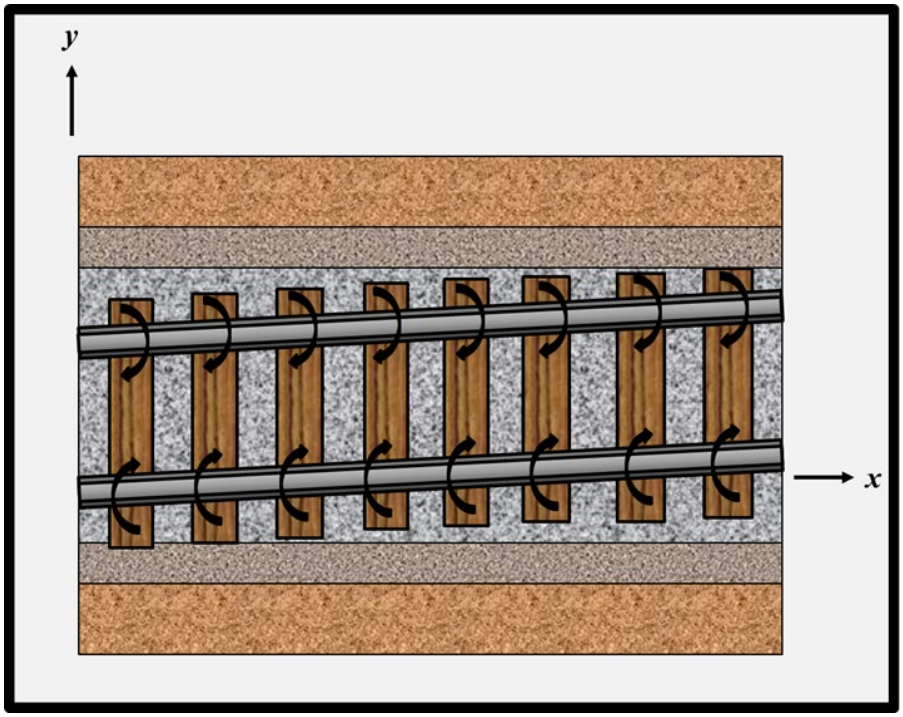

Figure 6: Demonstration of the rotational resistance induced by fasteners and ties (reprinted with permission from Allen and Fry, 2017)

Similar to the axial resistance, the precise amount of rotational resistance that is provided by the fastener as a function of the rotation angle (θ_z) is still unclear. In addition, the relationship may also be nonlinear and strongly dependent on the fastener type (Samavedam et al., 1993). In the current research, it is assumed that the rotational stiffness (S) is a constant as shown in Equation

(7). To facilitate implementation in the finite element model, the point moment (T_z) is reformulated as a distributed moment by dividing by d_{tie}. This approach, analogous to the treatment of tie–ballast resistance, results in a moment per unit length (τ_z), as expressed below.

$$T_z(\theta_z) = -S \cdot \theta_z \tag{7}$$

$$\tau_z(\theta_z) = \frac{T_z}{d_{tie}} \tag{8}$$

Rail buckling is typically triggered by thermal effects such as elevated ambient temperatures, direct solar exposure, and frictional heating from train operation. As a result, the thermal stresses arising from rail expansion must be accounted for in the analysis. In this study, heat transfer effects are not modeled directly, and it is assumed that the rail undergoes uniform temperature changes with no local variation. A linear thermoelastic constitutive relationship is employed in the model and is expressed as follows:

$$\sigma_{xx} = E(\varepsilon_{xx} - \alpha \cdot \Delta T) \tag{9}$$

Here, E is the Young's modulus, ε_{xx} is the axial strain, α is the coefficient of thermal expansion, and ΔT is the current temperature difference compared to the rail neutral temperature (RNT), implying that at RNT there will be no thermal stress applied to the system.

Finally, additional sources of loads or moments—such as those induced by vehicle operation—are represented as either distributed or concentrated point loads applied directly to the track structure. The influence of these external loadings on rail buckling behavior will be discussed in later sections.

2.3. Boundary Value Problem

Given the slender geometry of the rail—where the axial length greatly exceeds the lateral and vertical dimensions—the Euler-Bernoulli beam assumption is adopted. This assumption states that cross-sections of the rail remain planar and perpendicular to the centroidal axis throughout deformation. Based on this assumption, two key simplifications follow: (1) the transverse normal stress components are negligible compared to the axial stress; and (2) the displacement fields are functions of the axial coordinate x only (Euler, 1744; Allen and Haisler, 1985; Grissom and Kerr, 2006). According to field observations, torsional effects—specifically rotation about the x-axis—are relatively minor in the context of rail buckling. As such, a three-dimensional beam model with five degrees of freedom, excluding torsion, is developed in this study.

Under the Euler-Bernoulli framework, the effects of the stress components σ_{xx}, σ_{yy}, σ_{zz}, σ_{xy}, and σ_{xz}, are represented using the corresponding resultants: axial force (P), shear forces (V_y, V_z), and bending moments (M_y, M_z). The associated free-body diagrams are illustrated in Figure 7 and Figure 8.

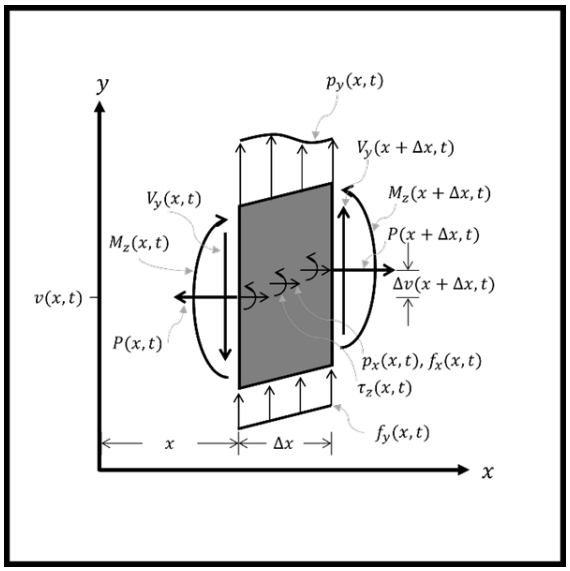

Figure 7: x-y plane view of the resultant forces and moment applied to a differential element of the rail (reprinted with Permission from Liu, 2025)

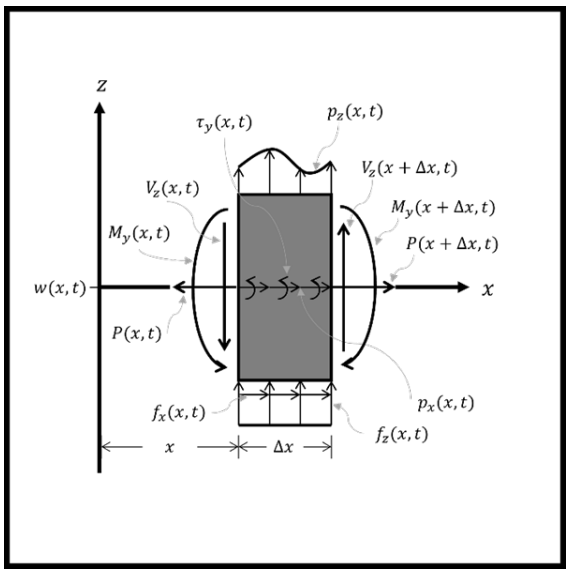

Figure 8: x-z plane view of the resultant forces and moment applied to a differential element of the rail (reprinted with Permission from Liu, 2025)

Here, u, v, w represent centroidal displacements in the x, y, z direction, p_x, p_y, p_z are the distributive loads applied to the element. With z^* defined as the vertical distance from the rail base to its centroid, the distributed moment produced by f_x is denoted by τ_y and can be obtained by:

$$\tau_y(x) = z^* \cdot f_x(x) \tag{10}$$

Note that the x-y plane is illustrated in its deformed configuration, whereas the x-z plane is kept undeformed. Owing to the disparity between the moments of inertia I_{yy} and I_{zz}, buckling

is far more prevalent in the x-y plane, and its geometric nonlinearity is therefore the primary focus of this study. Vertical buckling mostly arises when lateral motion is constrained, which seldom occurs, so significant vertical deflections are considered negligible and are not examined further in this research.

As buckling problems could induce large deformations, the axial strain-displacement relation is given by:

$$\varepsilon_{xx} = \frac{du}{dx} + \frac{1}{2}\left[\left(\frac{du}{dx}\right)^2 + \left(\frac{dv}{dx}\right)^2 + \left(\frac{dw}{dx}\right)^2\right] \tag{11}$$

as we know, lateral displacements are much more significant than the other two directions for the lateral bucking problem, $\frac{1}{2}\left(\frac{dv}{dx}\right)^2$ will be the only second-order term that needs to be taken into consideration (Tvergaard and Needleman, 1981; Grissom and Kerr, 2006), so that the final strain-displacement relationship utilized herein is therefore simplified as:

$$\varepsilon_{xx} = \frac{du}{dx} + \frac{1}{2}\left(\frac{dv}{dx}\right)^2 \tag{12}$$

Because the track length is much greater than the deflection amplitude, the rotational angles can be assumed to be small and expressed as:

$$\theta_y \cong tan(\theta_y) = -\lim_{\Delta x \to 0} \frac{\Delta w}{\Delta x} = -\frac{dw}{dx} \tag{13}$$

$$\theta_z \cong tan(\theta_z) = \lim_{\Delta x \to 0} \frac{\Delta v}{\Delta x} = \frac{dv}{dx} \tag{14}$$

With all the assumptions given, a well-posed initial boundary value problem can be constructed. By assuming that the problem is quasi-static and using standard time-stepping procedures, the only independent variable for solving the displacement fields at the centroid for each time-step will be x. Applying the equilibrium equations and utilizing the equations above, the problem shown in Table 1:

Table 1: Initial boundary value problem for predicting rail response (reprinted with Permission from Liu, 2025)

1. Independent variables: x

2. Known inputs:

Loads: $p_x = p_x(x), p_y = p_y(x), p_z = p_z(x), 0 < x < L$

Temperature change: ΔT, known

Geometry: A, I_{yy}, I_{zz}, L, z^*

Material properties: E, α

Track parameters: k_x, $F_{y,lt}$, $F_{y,pk}$, v_{lt}, v_{pk}, λ_x, λ_y, d_{tie}, k_z, S

3. Dependent variables: $u = u(x), v = v(x), w = w(x), P = P(x),$

$$V_y = V_y(x), V_z = V_z(x), M_y = M_y(x), M_z = M_z(x)$$

4. Field equations:

$$\frac{dP}{dx} = -p_x - f_x \tag{15}$$

$$\frac{dV_y}{dx} = -p_y - f_y \tag{16}$$

$$\frac{dV_z}{dx} = -p_z - f_z \tag{17}$$

$$\frac{dM_y}{dx} = V_z + z^* f_x \tag{18}$$

$$\frac{dM_z}{dx} = -V_y + P\frac{dv}{dx} - \tau_z \tag{19}$$

$$\frac{du}{dx} = \frac{P + P^T}{EA} - \frac{1}{2}\left(\frac{dv}{dx}\right)^2 \tag{20}$$

$$\frac{d^2v}{dx^2} = \frac{M_z}{EI_{zz}} \tag{21}$$

$$\frac{d^2w}{dx^2} = -\frac{M_y}{EI_{yy}} \tag{22}$$

5. Auxiliary equations: $f_x(u), f_y(v), f_z(w), \tau_z(\theta_z), P^T(\Delta T)$

The system includes 8 primary equations along with 5 auxiliary expressions accounting for tie-ballast resistance, vertical ballast support, fastener rotational stiffness, and loading from the thermoelastic constitutive relation. These collectively govern 8 dependent variables. While the problem is mathematically well-posed, the strong coupling among the equations makes it challenging to derive analytical solutions without introducing significant simplifications. To avoid such limitations, a finite element–based numerical solution approach is adopted in this study.

2.4. Finite Element Method

To solve the coupled equations in Table 1, we apply the principle of virtual work to Equations (15), (16) and (17), which are Newton's Law of Motion equations for the x, y, and z direction:

$$\int_0^L \left[\frac{dP}{dx} + p_x + f_x\right] \delta u \, dx + \int_0^L \left[\frac{dV_y}{dx} + p_y + f_y\right] \delta v \, dx + \int_0^L \left[\frac{dV_z}{dx} + p_z + f_z\right] \delta w \, dx = 0 \tag{23}$$

Through a series of integration by parts and equation substitution, we can come up with the final weak form of our problem:

$$\begin{aligned} &- \int_0^L EA \frac{du}{dx} \delta \frac{du}{dx} \, dx - \int_0^L EI_{zz} \frac{d^2v}{dx^2} \delta \frac{d^2v}{dx^2} \, dx - \int_0^L EI_{yy} \frac{d^2w}{dx^2} \delta \frac{d^2w}{dx^2} \, dx \\ &- \int_0^L \frac{EA}{2} \left(\frac{dv}{dx}\right)^2 \delta \frac{du}{dx} \, dx - \int_0^L EA \frac{du}{dx} \frac{dv}{dx} \delta \frac{dv}{dx} \, dx \\ &- \int_0^L \frac{EA}{2} \left(\frac{dv}{dx}\right)^3 \delta \frac{dv}{dx} \, dx + \int_0^L P^T \, \delta \frac{du}{dx} \, dx + \int_0^L P^T \frac{dv}{dx} \delta \frac{dv}{dx} \, dx \\ &+ \int_0^L f_x \, \delta u \, dx + \int_0^L f_y \, \delta v \, dx + \int_0^L f_z \, \delta w \, dx + \int_0^L z^* f_x \, \delta \frac{dw}{dx} \, dx \\ &+ \int_0^L \tau_z \, \delta \frac{dv}{dx} \, dx + \int_0^L p_x \, \delta u \, dx + \int_0^L p_y \, \delta v \, dx + \int_0^L p_z \, \delta w \, dx \\ &+ [P \, \delta u]_0^L + \left[V_y \, \delta v\right]_0^L + [V_z \, \delta w]_0^L + \left[M_y \, \delta \theta_y\right]_0^L + [M_z \, \delta \theta_z]_0^L = 0 \end{aligned} \tag{24}$$

As shown, the system includes multiple sources of nonlinearity: geometric nonlinearity (terms 5 and 6), nonlinearity from the strain–displacement relationship (terms 4 and 6), and the nonlinear behavior of lateral tie–ballast resistance (term 10). Additionally, although not explicitly included in the weak formulation, nonlinear effects from point loads and moments are incorporated through realistic boundary conditions.

To solve the weak form with the finite element method, we employ Hermite shape functions of cubic order (Allen and Haisler, 1985):

Substituting into the weak formulation, we have:

$$\sum_{i=1}^{10} (I_i^e - F_i^e) \, \delta q_i^e = 0 \tag{25}$$

$$\boldsymbol{q}^e = [u_1^e \quad v_1^e \quad w_1^e \quad \theta_{y,1}^e \quad \theta_{z,1}^e \quad u_2^e \quad v_2^e \quad w_2^e \quad \theta_{y,2}^e \quad \theta_{z,2}^e]^T \tag{26}$$

where:

$$I_i^e = I_{Lin,i}^e + I_{LS,i}^e + I_{Geo,i}^e + I_{LS,Geo,i}^e + I_{T,i}^e + I_{Lon,i}^e + I_{Lat,i}^e + I_{Bal,i}^e + I_{Fas,i}^e \tag{27}$$

$$F_i^e = \int_0^{L^e} \left[p_x \xi_i + p_y \eta_i + p_z \zeta_i + P^T \frac{d\xi_i}{dx} \right] dx \tag{28}$$

In this context, I_i^e is a functional that depends on the functions defined by the displacement array (q_i^e), while F_i^e represents the force vector that accounts for external loads or temperature effects. The components of I_i^e are listed below:

$$\begin{aligned} I_{Lin,i}^e = \int_0^{L^e} [\, & EA \frac{d}{dx}\left(\sum_{m=1}^{10} \xi_m \, q_m^e\right)\frac{d\xi_i}{dx} + EI_{zz}\frac{d^2}{dx^2}\left(\sum_{m=1}^{10} \eta_m \, q_m^e\right)\frac{d^2\eta_i}{dx^2} \\ & + EI_{yy}\frac{d^2}{dx^2}\left(\sum_{m=1}^{10} \zeta_m \, q_m^e\right)\frac{d^2\zeta_i}{dx^2}]dx \end{aligned} \tag{29}$$

$$I_{LS,i}^e = \int_0^{L^e} \left[\frac{EA}{2} \frac{d}{dx}\left(\sum_{m=1}^{10} \eta_m \, q_m^e\right)\frac{d}{dx}\left(\sum_{n=1}^{10} \eta_n \, q_n^e\right)\frac{d\xi_i}{dx} \right] dx \tag{30}$$

$$I_{Geo,i}^e = \int_0^{L^e} \left[EA \frac{d}{dx}\left(\sum_{m=1}^{10} \xi_m \, q_m^e\right)\frac{d}{dx}\left(\sum_{n=1}^{10} \eta_n \, q_n^e\right)\frac{d\eta_i}{dx} \right] dx \tag{31}$$

$$I_{LS,Geo,i}^e = \int_0^{L^e} \left[\frac{EA}{2} \frac{d}{dx}\left(\sum_{m=1}^{10} \eta_m \, q_m^e\right)\frac{d}{dx}\left(\sum_{n=1}^{10} \eta_n \, q_n^e\right)\frac{d}{dx}\left(\sum_{r=1}^{10} \eta_r \, q_r^e\right)\frac{d\eta_i}{dx} \right] dx \tag{32}$$

$$I_{T,i}^e = -\int_0^{L^e} \left[P^T \frac{d}{dx}\left(\sum_{m=1}^{10} \eta_m \, q_m^e\right)\frac{d\eta_i}{dx} \right] dx \tag{33}$$

$$I_{Lon,i}^e = -\int_0^{L^e} f_x \, \xi_i \, dx - \int_0^{L^e} z^* f_x \frac{d\zeta_i}{dx} \, dx \tag{34}$$

$$I_{Lat,i}^{e} = -\int_{0}^{L^e} f_y \, \eta_i \, dx \tag{35}$$

$$I_{Bal,i}^{e} = -\int_{0}^{L^e} f_z \, \zeta_i \, dx \tag{36}$$

$$I_{Fas,i}^{e} = -\int_{0}^{L^e} \tau_z \, \frac{d\eta_i}{dx} \, dx \tag{37}$$

Here, $I_{Lin,i}^{e}$ includes the linear contributions from axial and bending stiffness. The terms $I_{LS,i}^{e}$ represent large strain effects in the axial direction. $I_{Geo,i}^{e}$ captures geometric nonlinearity, while $I_{LS,Geo,i}^{e}$ accounts for the combined influence of geometric nonlinearity under large strain conditions. The terms $I_{T,i}^{e}$, $I_{Lon,i}^{e}$, $I_{Lat,i}^{e}$, $I_{Bal,i}^{e}$, $I_{Fas,i}^{e}$ correspond to secondary moment effects from thermal loads, longitudinal tie-ballast resistance, lateral tie-ballast resistance, vertical ballast support, and fastener rotational resistance, respectively. The resultant force and moment terms at the boundaries are intentionally excluded, since they cancel out during the process of assembling the local forms into the global system.

Since δq_i should be mutually linear independent, and Equation (25) is always true, we obtain a set of 10 equations:

$$I_i^e = F_i^e, \text{ for } i = 1 \text{ to } 10 \tag{38}$$

Since the problem involves nonlinearities that require a time-stepping approach, a Taylor expansion of $I_i^e(q_j)$ is performed. By omitting higher-order terms, the resulting incremental equilibrium equations are derived as follows:

$$K_{ij}^{e} \Delta q_j^e = \Delta F_i^e \tag{39}$$

$$K_{ij}^{e} = \frac{\partial I_i^e}{\partial q_j^e} \tag{40}$$

$$\Delta F_i^e = F_i^e\left(q_j^e + \Delta q_j^e\right) - F_i^e\left(q_j^e\right) \tag{41}$$

Here, K_{ij}^{e} is the Jacobian matrix of I_i^e, commonly known as the element stiffness matrix in the finite element method. Rather than using numerical integration techniques such as Gauss

quadrature to compute the coefficients of K_{ij}^{e}, these values are precomputed to reduce computational cost. Further details can be found in Liu (2025).

Utilizing the standard FE assembly method, the local stiffness matrices and force vectors are assembled into the global form to model the entire rail section.

2.5. Buckling Load Identification

To accurately capture the nonlinear behavior of K_{ij}, which is the global stiffness matrix that depends on the global displacement vector (q_j), the entire loading process is divided into multiple time-steps. When the load increment (ΔF_i) is specified at each step, the corresponding displacement field (q_j) can be obtained using Equation (38). This procedure is known as the force-control algorithm. It has been verified against several analytical solutions and has proven effective in predicting the critical buckling load (P_{cr}), which refers to the axial load at the first point of instability, across a range of scenarios (Musu, 2021, 2023; Liu, 2025). P_{cr} can be identified by looking at the applied axial load vs. maximum lateral displacement curve, as shown in Figure 9:

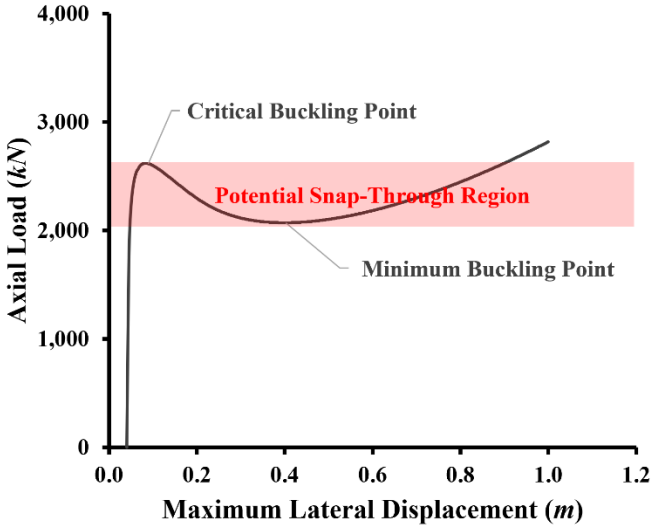

Figure 9: Demonstration of the axial load vs. maximum lateral displacement curve for a rail buckling problem (reprinted with Permission from Liu, 2025)

In symmetric buckling problems without external loads, the maximum lateral displacement occurs at the midpoint of the rail, and the corresponding load represents the compressive thermal force applied simultaneously at both ends of the track system.

In many cases, as the applied load increases and exceeds P_{cr}, the slope of the load–displacement curve drops sharply, a behavior known as softening. In reality, the displacement path often exhibits snap-through at the first unstable point, where the applied load reaches a local maximum and does not exist an equilibrium state with a larger axial load value close to the critical buckling point. However, if additional energy enters the system—such as dynamic loads from passing vehicles—the rail may buckle under lower axial loads (Kish and Samavedam, 2013). At larger displacement values, the curve may stiffen again, likely due to nonlinear large strain effects.

This creates a snap-through region, with the lowest point referred to as the minimum buckling load (P_{min}), as illustrated in Figure 9.

Because the force-control algorithm cannot accommodate negative load increments, it fails to capture the full equilibrium path once softening occurs beyond the critical buckling point. To address this, the displacement-control algorithm is used in this study.

2.6. Displacement-Control Algorithm

The displacement-control algorithm works by incrementally increasing the displacement at a designated point and computing the corresponding axial load needed to achieve that change. In this study, the buckling shape is assumed to be symmetric about the midpoint, so the midpoint—where the maximum lateral displacement occurs—is chosen as the control point. Since parts of both the displacement and force vectors are unknown, the problem is classified as one with mixed boundary conditions. The displacement-control algorithm herein is based on the self-correcting displacement incrementation method proposed by Stricklin, Haisler, and Key (1977), with modifications made to suit the specific requirements of rail buckling analysis.

The displacement control procedure starts with the assembled global form of element-wise Equation (39):

$$K_{ij}^{old} \Delta q_j^1 = \Delta F_i^1 \tag{42}$$

Here, the superscript "old" indicates that the stiffness matrix (K_{ij}) is known a-priori based on initial conditions or results of the previous time-step; the superscript "1" indicates that this equation is currently used for the first iteration.

By dividing Equation (42) into sub-matrices and vectors, it can be rewritten as:

$$K_{ff,ij}^{old} \Delta q_{f,j}^1 + K_{fc,ij}^{old} \Delta q_{c,j}^1 = \Delta F_{f,i}^1 = \Delta P^1 f_{f,i} \tag{43}$$

$$K_{cf,ij}^{old} \Delta q_{f,j}^1 + K_{cc,ij}^{old} \Delta q_{c,j}^1 = \Delta F_{c,i}^1 = \Delta P^1 f_{c,i} \tag{44}$$

In this formulation, the subscripts f and c refer to the "free" and "constrained" degrees of freedom, respectively. The vector $\Delta q_{f,j}^1$ contains the displacement changes for nodes that are free to vary during the simulation. In contrast, $\Delta q_{c,j}^1$ contains prescribed displacement changes, defined by the displacement boundary conditions and the displacement control point, and is therefore known. ΔP^1 is a scalar representing the applied load magnitude. The vectors $f_{f,i}$ and $f_{c,i}$ consist of entries with values of 0 or 1, indicating the locations where load increments are applied. Since the location and direction of the external loads are given, $f_{f,i}$ and $f_{c,i}$ can be treated as known variables throughout the calculation

Rearranging Equation (43), $\Delta q_{f,j}^1$ can be written as:

$$\Delta q_{f,j}^{1} = A_j + \Delta P^1 B_j \tag{45}$$

Here, A_j and B_j are defined by the following systems of equations:

$$K_{ff,ij}^{old} A_j = -K_{fc,ij}^{old} \Delta q_{c,j}^{1} \tag{46}$$

$$K_{ff,ij}^{old} B_j = f_{f,i} \tag{47}$$

By solving A_j and B_j and substituting them into Equation (45), $\Delta q_{f,j}^{1}$ can be expressed as a function of ΔP^1. Substituting this expression into Equation (44) leads to:

$$\Delta P^1 \left(K_{cf,ij}^{old} B_j - f_{c,i}\right) = -K_{cf,ij}^{old} A_j - K_{cc,ij}^{old} \Delta q_{c,j}^{1} \tag{48}$$

Since both sides of Equation (48) are vectors of the same dimension, element-wise division is used to calculate ΔP^1.

Using the predefined $\Delta q_{c,j}^{1}$, $f_{c,i}$, and $f_{f,i}$, along with the computed values of $\Delta q_{c,j}^{1}$ and ΔP^1, the global displacement change vector Δq_j^1 and the global load change vector ΔF_i^1 for the first iteration can be assembled. With K_{ij}^1 updated using Δq_j^1, the force residual, R_i^1 is then calculated through Equation (49) shown below, completing the calculation for the first iteration.

$$R_i^1 = R_i\left(\Delta q_j^1\right) = K_{ij}^1 \Delta q_j^1 - \Delta F_i^1 \tag{49}$$

where:

$$K_{ij}^1 = K_{ij}\left(q_j^1\right) \tag{50}$$

$$q_j^1 = q_{j,old} + \Delta q_j^1 \tag{51}$$

In this context, $q_{j,old}$ refers to the global displacement vector from the previous time-step. The goal of the iteration is to reduce the residual—representing the imbalance between the applied load and the internal reaction force resulting from the current displacement update—to a sufficiently small value, indicating that equilibrium has been achieved.

If the magnitude of the residual vector $\left|\left|R_i^1\right|\right|$ does not meet the predefined convergence criterion, the iteration continues. For iteration $m > 1$, the updated displacement Δq_j^m and load increment ΔF_i^m are computed using:

$$K_{ij}^{m-1}\Delta q_j^m = \Delta F_i^m \tag{52}$$

To simplify the formulation, the displacement correction vector ($\Delta\Delta q_j^m$) and force correction vector ($\Delta\Delta F_i^m$) are introduced as:

$$\Delta\Delta q_j^m = \Delta q_j^m - \Delta q_j^{m-1} \tag{53}$$

$$\Delta\Delta F_i^m = \Delta F_i^m - \Delta F_i^{m-1} \tag{54}$$

Substituting into Equation (52), the system becomes:

$$K_{ij}^{m-1}\Delta\Delta q_j^m = \Delta\Delta F_i^m - R_i^{m-1} \tag{55}$$

This equation is solved using the same procedure described in Equations (42) to (48), and the process is repeated until the convergence criterion is satisfied.

The displacement-control algorithm allows the simulation to continue through the softening phase of rail buckling. As mentioned before, the point at which the curve's slope changes direction is defined as the minimum buckling point, associated with the minimum buckling load (P_{min}) and the corresponding lateral displacement (v_{min}). This point is significant because applied axial loads below P_{min} are insufficient to cause buckling, even with additional external energy, as no stable equilibrium configuration exists under such conditions.

2.7. Model Verification

Given the highly nonlinear and complex nature of rail buckling, direct validation against real-world scenarios is challenging. Therefore, the model is verified using simplified cases with known analytical solutions. Since the force-control algorithm implemented here has already been validated against several analytical benchmarks and demonstrated to be reliable (Musu et al., 2021, 2023; Liu, 2025), the results from the displacement-control algorithm are compared against those from the force-control approach to assess its accuracy and consistency.

The Euler buckling problem is used as a demonstration to verify the displacement-control algorithm. For this purpose, a linear strain–displacement relationship is adopted to simplify the analytical derivation. This condition is implemented in the FEM code via a user-defined flag that allows switching between linear and nonlinear strain formulations.

Verification Setup:

A rail is subjected to an axial point load P applied at the left end ($x = 0$). Both ends are simply supported, but axial displacement is allowed at $x = 0$, as illustrated in Figure 10. The rail properties are: $L = 10\ m$, $E = 2.06 \times 10^{11}\ N/m^2$, $A = 0.0172\ m^2$, $I_{zz} = 1.22 \times 10^{-5}\ m^4$. Tie–ballast resistances and fastener rotational resistance are neglected in this case to align with the analytical assumptions.

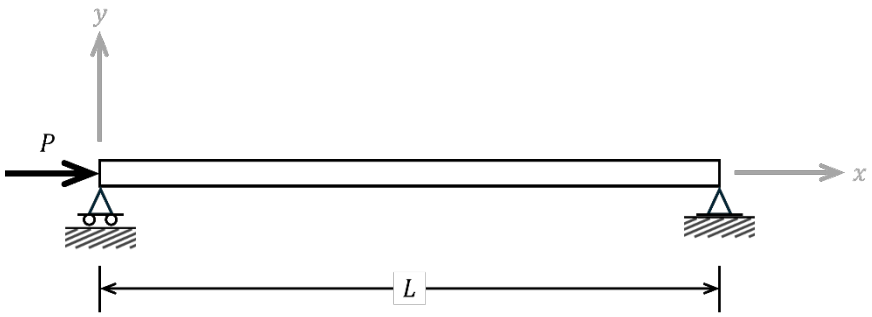

Figure 10: Depiction of the displacement-control algorithm verification problem (reprinted with Permission from Liu, 2025)

Objective:

Determine the analytical buckling load and compare it with FEM predictions using both the force-control and displacement-control algorithms.

Analytical Solution:

Using the classical Euler buckling formula for a pinned–pinned beam:

$$P_{cr} = \frac{\pi^2 \, E \, I_{zz}}{L^2} \tag{56}$$

The resulting critical load is $P_{cr} = 248.8 \, kN$.

FEM Simulation:

To capture geometric nonlinearity, a small initial imperfection is introduced at the rail midpoint. Its magnitude is kept small enough to avoid affecting the critical load prediction. Both FEM simulations use 20 equally spaced beam elements.

Figure 11 shows the load–displacement curves produced by the two algorithms. The displacement-control results closely match both the force-control solution and the analytical benchmark, confirming the accuracy of the displacement-control algorithm for nonlinear buckling analysis.

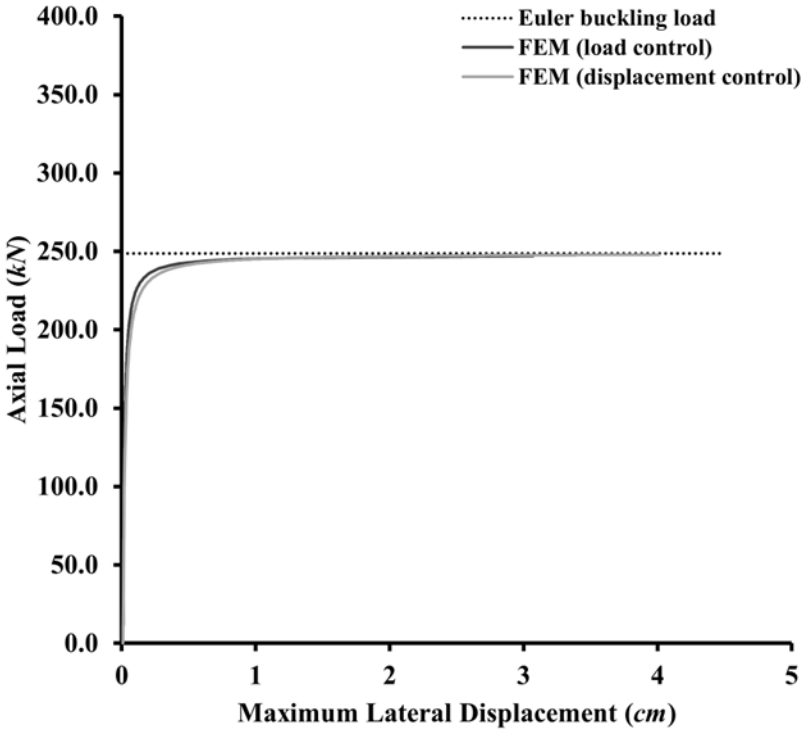

Figure 11: Result of the applied axial load vs. maximum displacement curves for different solving procedures (reprinted with Permission from Liu, 2025)

3. Results and Sensitivity Studies

This section presents the results of displacement-control simulations, and a sensitivity study focused on one of the key parameters affecting rail buckling: lateral tie–ballast resistance. As the lateral resistance can be described by several different parameters, the objective is to use the developed algorithm to assess how variations in these factors influence the critical buckling load and the corresponding lateral displacements, and demonstrate the capability of the computer model.

3.1. Problem Setup

While parametric studies are conducted by modifying one specific factor at a time, a base case is first defined. The base case is constructed using realistic rail and track properties, primarily based on the AREMA 136RE rail profile. Cross-sectional area and moments of inertia are doubled to represent a two-rail system. Steel material properties are taken from standard industry specifications (Nippon Steel Corporation, 2020; Musu, 2021). For this study, the ballast condition is assumed to be disturbed as it is more prone to buckle, and lateral tie–ballast resistance is modeled using a bilinear force–displacement relationship.

Buckling simulations are conducted on a constrained rail section with a predefined buckling length (L). Both ends are fixed against lateral and vertical displacements as well as rotations, including in the $x-y$ plane, while axial contraction or expansion is permitted throughout the misalignment and buckling process. Mechanical axial loads are applied at both ends

to induce buckling, representing the effect of thermal loads resulting from temperature increases relative to the rail neutral temperature, as defined by Equation (9).

To initiate buckling, initial lateral geometric imperfections are introduced by applying a small lateral point load at midspan. This procedure can be performed using either the force-control or displacement-control algorithm. After the misalignment is imposed as shown in Figure 12, displacement values used for computing axial, lateral and rotational resistance in Equation (4), (5) and (8) are reset to zero to simulate a static, misaligned initial state. It is important to allow axial freedom during this stage, as constraining both ends axially during misalignment would effectively pre-tension the rail and lead to an overestimation of the critical buckling load, potentially misrepresenting the system's safety margin.

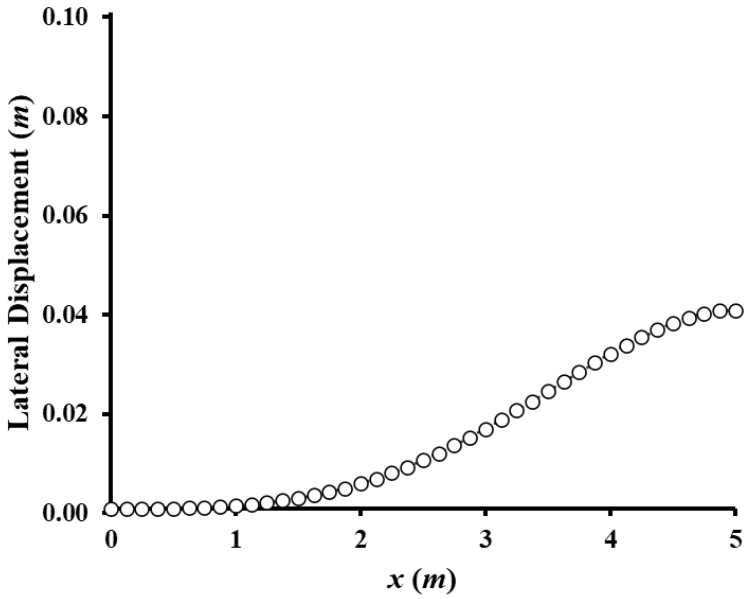

Figure 12: Illustration of the lateral displacements along half of the rail when it is misaligned (reprinted with Permission from Liu, 2025)

Table 2 lists all input parameters for the base case in SI units. Although the values are chosen to reflect realistic conditions, they may vary in practice and are primarily intended to showcase the functionality of the code.

Table 2: Base case input parameters for the sensitivity study (SI units) (reprinted with Permission from Liu, 2025)

Input Parameter	**Value**	**Unit**
Rail Buckling Length, L	10.00	m
Cross-Section, $2A$	1.72×10^{-2}	m^2
Moment of Inertia, $2I_{yy}$	7.90×10^{-5}	m^4
Moment of Inertia, $2I_{zz}$	1.22×10^{-5}	m^4
Rail Weight Per Unit Length, $2n_{rail}$	1.32×10^{3}	N/m
Modeled Tie-Weight, N_{tie}	1.00×10^{3}	N
Modeled Friction Coefficient, μ	1.50	
Rail Young's Modulus, E	2.06×10^{11}	N/m^2
Rail Thermal Expansion Coefficient, α	1.05×10^{-5}	$1/°C$
Tie-Spacing, d_{tie}	0.50	m
Longitudinal Tie-Ballast Resistance Coefficient, k_x	2.00×10^{6}	N/m
STPT Limit Lateral Force, $F_{y,lt}$	1.00×10^{4}	N
STPT Limit Lateral Displacement, v_{lt}	5.00×10^{-3}	m
Track Modulus, k_z	7.00×10^{7}	N/m^2
Fastener Rotational Stiffness, S	2.25×10^{5}	$N \cdot m/rad$
STPT Tie-Weight, $N_{tie,STPT}$	1.00×10^{3}	N
STPT Friction Coefficient, μ_{STPT}	1.50	
Misalignment Value, d_{mis}	4.00×10^{-2}	m

3.2. Convergence Studies

To ensure numerical accuracy, mesh and step size convergence were examined prior to the sensitivity analysis (Liu, 2025). A uniform mesh of 0.25 m per element length and a displacement step size of 8×10^{-4} m were found to produce minimum buckling load and corresponding displacement results within 2% of finer settings and are used throughout the study.

3.3. Sensitivity Study: Lateral Tie–Ballast Resistance

Given the highly nonlinear behavior of lateral tie–ballast resistance (hereafter referred to as lateral resistance), two scenarios are examined. In both cases, the resistance is defined by a bilinear relationship characterized by two parameters: the limit lateral force ($F_{y,lt}$) and the corresponding limiting displacement (v_{lt}), representing disturbed ballast conditions.

3.3.1. Case 1: Variation in Limit Force

In the first case, $F_{y,lt}$ varies from 0 to 20 kN to examine its influence on buckling behavior. The load–displacement curves in Figure 13 show that increasing $F_{y,lt}$ substantially raises both the P_{cr} and P_{min}, highlighting the pivotal role of lateral resistance in rail stability. As $F_{y,lt}$ decreases, the difference between P_{cr} and P_{min} narrows, indicating a reduced softening effect and a transition from snap-through buckling to progressive buckling. In the extreme case of $F_{y,lt} = 0$, the load–displacement response becomes fully progressive, with no distinguishable peak or softening region. Although a sharp buckling threshold is absent in this case, the axial load required to induce large lateral displacements remains significantly lower than in all other scenarios, emphasizing the vulnerability of such degraded conditions.

As shown in Figure 14, the values of P_{cr} and P_{min} rise nonlinearly with increasing $F_{y,lt}$, but the gap between them also becomes more pronounced, reflecting a clearer onset of instability as lateral restraint improves. It is important to note that the $F_{y,lt} = 0$ case is omitted from Figure 14, as the absence of a discernible critical point makes it difficult to define either buckling load.

Additionally, except for the $F_{y,lt} = 0$ case, all other load–displacement curves in Figure 13 are plotted only up to their respective P_{min} points. This is because, beyond P_{min}, the displacement-control algorithm reveals a secondary stiffening response, where the axial load begins to increase again with further displacement. This post-buckling behavior is not included in the figure to avoid confusion and to better emphasize the initial buckling characteristics under varying lateral resistance conditions.

These results are consistent with prior studies (Samavedam et al., 1993; Kish and Samavedam, 2013), which suggest that weak lateral resistance reduces the chance of snap-through and promotes a gradual, progressive buckling mode. Nonetheless, the drastically reduced load threshold underscores the importance of avoiding such ballast degradation in field conditions.

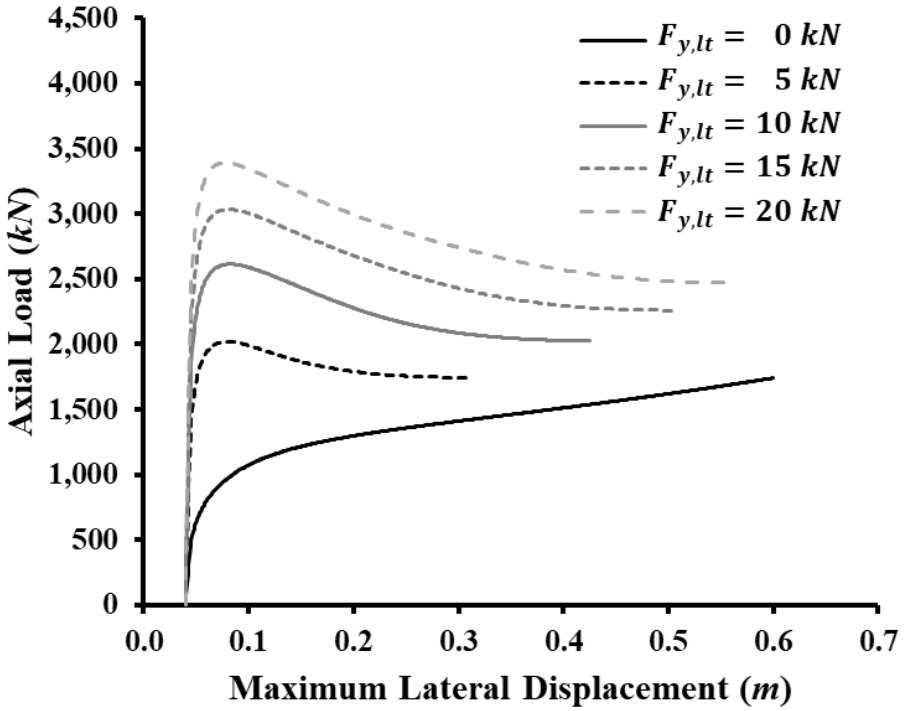

Figure 13: Maximum lateral displacement vs. applied axial load with various limit lateral resistance values applied to a typical rail structure

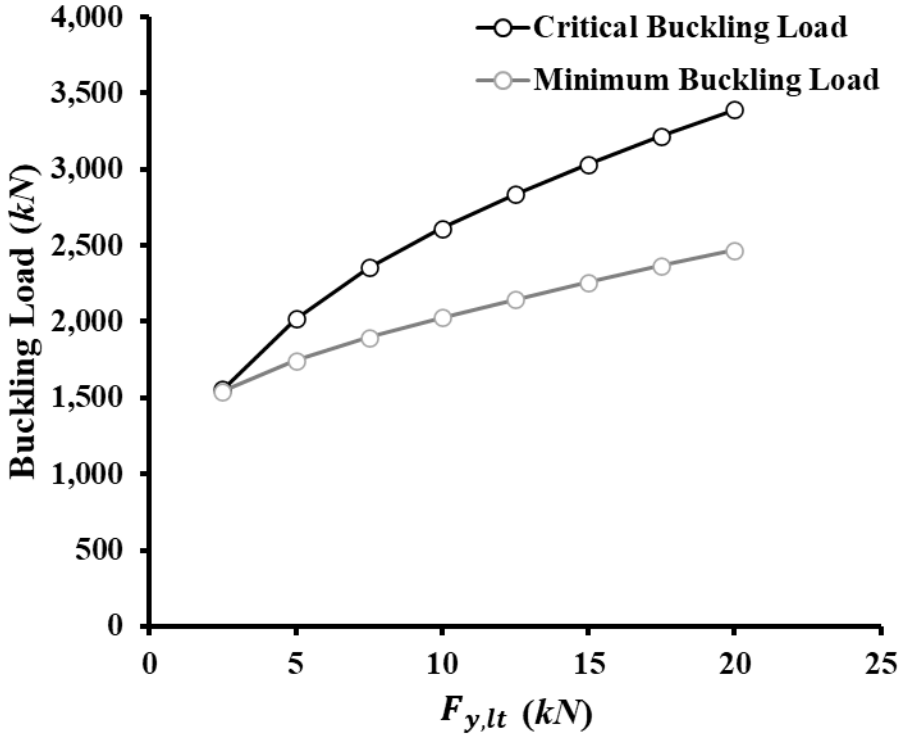

Figure 14: Predicted effect of changes in the limit lateral resistance value on buckling load of a typical rail structure

3.3.2. Case 2: Variation in Limit Displacement

In the second case, the limiting displacement v_{lt} varies from 0.25 cm to 0.75 cm. As shown in Figure 15, this parameter introduces slight differences in the initial slope of the load–displacement curves, and Figure 16 indicates small variations in both P_{cr} and P_{min}. However, the differences in the corresponding critical displacement values are minimal—typically just a few millimeters—and are not significant enough to warrant further investigation at the structural scale of rail buckling.

Moreover, such small differences in v_{lt} are difficult to capture reliably in practice, particularly during single-tie push test (STPT) experiments, where precise measurement of lateral displacement at the onset of limit resistance is inherently challenging. These findings suggest that, compared to the $F_{y,lt}$, v_{lt} has a much less pronounced influence on buckling performance and can be treated as a secondary parameter in design and evaluation.

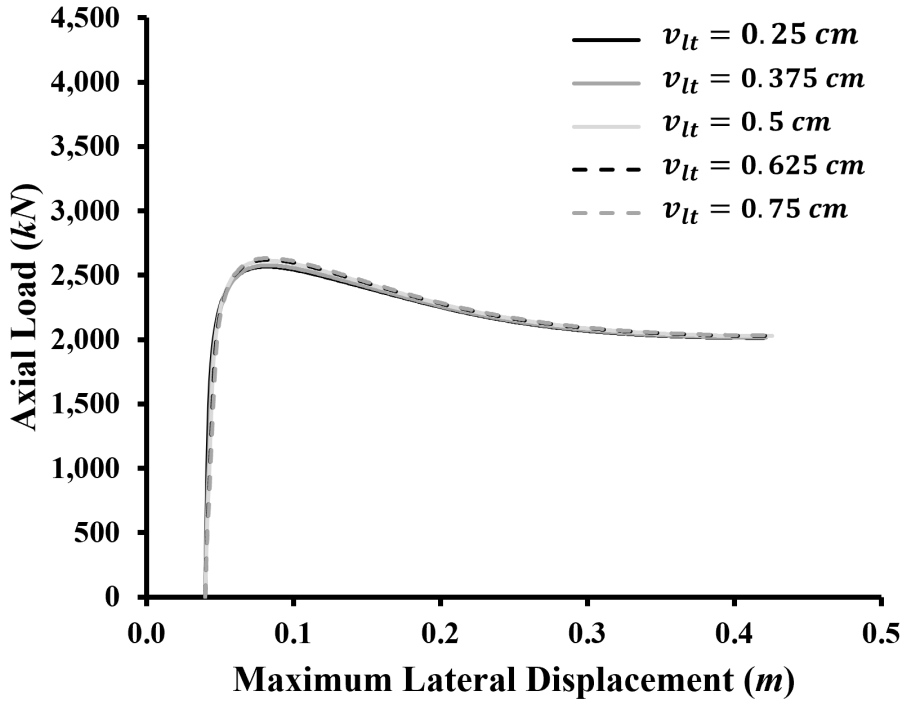

Figure 15: Maximum lateral displacement vs. applied axial load with various limit lateral displacement values applied to a typical rail structure (reprinted with Permission from Liu, 2025)

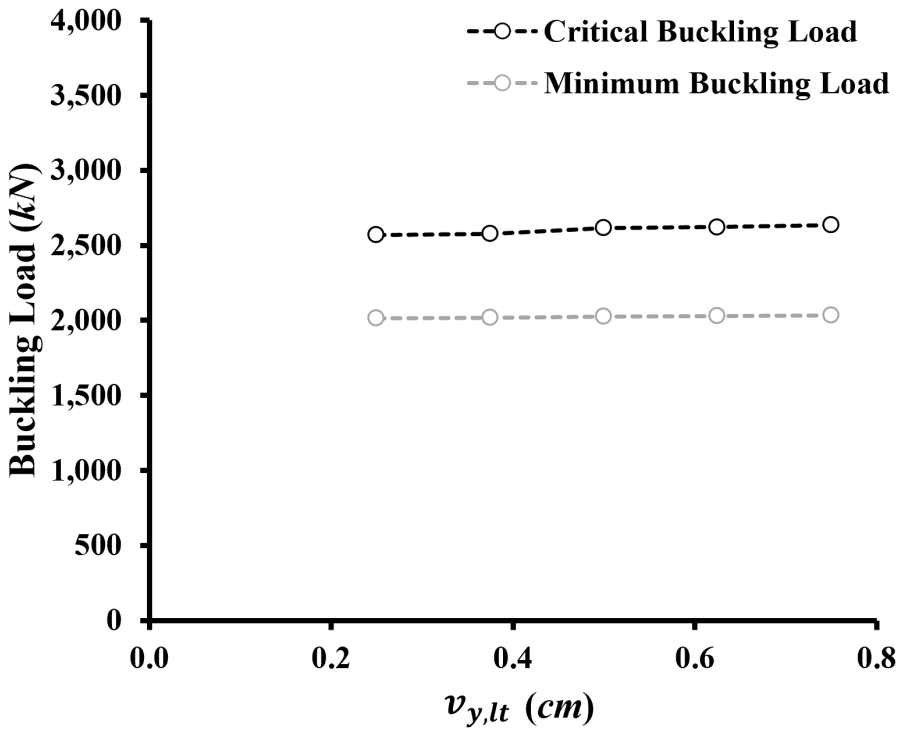

Figure 16: Predicted effect of changes in the limit lateral displacement value on buckling load of a typical rail structure (reprinted with Permission from Liu, 2025)

4. Conclusion

In this study, a nonlinear finite element model for predicting rail buckling was developed using a displacement-control approach. The model is designed to be computationally efficient and is capable of capturing both critical and post-buckling behavior, which is often missed in traditional force-controlled methods. A key feature of the framework is its flexibility—it allows displacement control to be applied at any degree of freedom, making it suitable for a wide range of buckling scenarios and boundary conditions.

Sensitivity studies were carried out to connect STPT experimental data to the model. The results confirm that the lateral tie-ballast resistance value plays a dominant role in determining buckling strength, with a nonlinear relationship observed across the tested range. In comparison, variation in the STPT limit displacement showed only small changes in response, particularly in terms of critical displacement values. These differences are minor and unlikely to impact buckling outcomes at the structural level. Moreover, such small differences are difficult to measure accurately in STPT experiments, so further investigation may not be warranted.

Moving forward, the displacement-control algorithm developed here can serve as a foundation for more advanced post-buckling analyses. It could be extended to handle train-induced dynamic effects or adapted for real-time stability assessment, especially in systems where lateral resistance conditions change over time.

References

Allen, D. H., & Fry, G. D. (2016). Analysis of a Rail Subjected to Mechanical and Thermal Loading. Report.

Allen, D. H., & Fry, G. D. (2016). Finite Element Formulation for Thermal Buckling of Rails. Report.

Allen, D. H., & Fry, G. D. (2017). Finite Element Formulation and Verification for Thermal Buckling of Rail Structures in the Horizontal Plane. Report.

Allen, D. H., & Haisler, W. E. (1985). Introduction to aerospace structural analysis. (No Title).

Braun, S. (2002, July 30). Passenger Train Cars Plunge Off Overheated Tracks. Retrieved from Los Angeles Times: https://www.latimes.com/archives/la-xpm-2002-jul-30-na-train30-story.html

Dong, R. G., Sankar, S., & Dukkipati, R. V. (1994). A finite element model of railway track and its application to the wheel flat problem. Proceedings of the Institution of Mechanical Engineers, Part F: Journal of Rail and Rapid Transit, 208, 61–72.

Euler, L. (1744). Methodus inveniendi Lineas Curvas.

Federal Railroad Administration, O. o. (2024). Train Accidents and Rates. Train Accidents and Rates, 2024. Retrieved from https://safetydata.fra.dot.gov/officeofSafety/publicsite/Query/TrainAccidentsFYCYWithRates.aspx

Galilei, G. (1638). Dialogues Concerning Two New Sciences.

Grissom, G. T., & Kerr, A. D. (2006). Analysis of lateral track buckling using new frame-type equations. International Journal of Mechanical Sciences, 48, 21-32. doi:https://doi.org/10.1016/j.ijmecsci.2005.09.006

Haisler, W. E., Stricklin, J. A., & Key, J. E. (1977). Displacement incrementation in non-linear structural analysis by the self-correcting method. International Journal for Numerical Methods in Engineering, 11, 3-10. doi:10.1002/nme.1620110103

Kerr, A. D. (1974). The stress and stability analyses of railroad tracks.

Kerr, A. D., & others. (1976). Analysis of thermal track buckling in the lateral plane. Tech. rep., United States. Federal Railroad Administration.

Kish, A., & Samavedam, G. (1991). Dynamic buckling of continuous welded rail track: Theory, tests, and safety concepts. Transportation Research Record, 1289, 23-38.

Kish, A., & Samavedam, G. (2013). Track buckling prevention: theory, safety concepts, and applications. Report, John A. Volpe National Transportation Systems Center (US).

Kish, A., Samavedam, G., & Jeong, D. Y. (1982). Analysis of thermal buckling tests on US railroads. Report, United States. Federal Railroad Administration.

Kish, A., Samavedam, G., Jeong, D. Y., & others. (1985). Influence of vehicle induced loads on the lateral stability of CWR track. Tech. rep., United States. Department of Transportation. Federal Railroad Administration.

Knoll, D. A., & Keyes, D. E. (2004). Jacobian-free Newton–Krylov methods: a survey of approaches and applications. Journal of Computational Physics, 193, 357-397.

Li, D., & Shust, W. (1997). Investigation of Lateral Track Strength and Track Panel Shift Using AAR's Track Loading Vehicle. Report.

Li, S.-R., & Batra, R. C. (2007). Thermal buckling and postbuckling of Euler-Bernoulli beams supported on nonlinear elastic foundations. AIAA journal, 45, 712–720.

Lim, N.-H., Park, N.-H., & Kang, Y.-J. (2003). Stability of continuous welded rail track. Computers & Structures, 81, 2219–2236.

Miri, A., Dhanasekar, M., Thambiratnam, D., Weston, B., & Chan, T. H. (2021). Analysis of buckling failure in continuously welded railway tracks. Engineering Failure Analysis, 119, 104989.

Musu, V. (2021). Computational Model for Predicting Buckling in Rail Structures. Thesis.

Musu, V. (2023). Development of a Model for the Prediction of the Effects of Multiple Distinct Modes of Nonlinearity on Rail Buckling. Thesis.

National Transportation Safety Board. (2003, August 5). Derailment of Amtrak Auto Train P052-18 on the CSXT Railroad near Crescent City, Florida, April 18, 2002 (Report No. RAR-03-02). Retrieved from https://www.ntsb.gov/investigations/AccidentReports/Reports/RAR0302.pdf

National Transportation Safety Board. (2004). Railroad accident brief: DCA-02-MR-005. Washington, D.C.: National Transportation Safety Board. Retrieved from https://www.ntsb.gov/investigations/AccidentReports/Reports/RAB0405.pdf

Nippon Steel Corporation. (2020). Rails. Retrieved from Rails: https://www.nipponsteel.com/product/catalog_download/pdf/K003en.pdf

Nobakht, S., Zakeri, J.-A., & Safizadeh, A. (2022). Investigation on longitudinal resistance of the ballasted railway track under vertical load. Construction and Building Materials, 317, 126074. doi:https://doi.org/10.1016/j.conbuildmat.2021.126074

Oden, J. T. (1967). Mechanics of elastic structures.

Pucillo, G. P. (2016). Thermal buckling and post-buckling behaviour of continuous welded rail track. Vehicle System Dynamics, 54, 1785–1807.

Saad, Y., & Schultz, M. H. (1986). GMRES: A Generalized Minimal Residual Algorithm for Solving Nonsymmetric Linear Systems. SIAM Journal on Scientific and Statistical Computing, 7, 856-869. doi:10.1137/0907058

Samavedam, G., Kanaan, A., Pietrak, J., Kish, A., Sluz, A., & others. (1995). Wood tie track resistance charaterization and correlations study. Tech. rep., United States. Department of Transportation. Federal Railroad Administration.

Samavedam, G., Kish, A., Purple, A., Schoengart, J., & others. (1993). Parametric Analysis and Safety Concepts of CWR Track Buckling. Tech. rep., United States. Federal Railroad Administration.

Stricklin, J. A., & Haisler, W. E. (1977). Formulations and solution procedures for nonlinear structural analysis. Computers & Structures, 7, 125-136.

Timoshenko, S. (1915). Strength of rails. Transactions of the Institute of Ways and Communications, St. Petersburg, Russia.

Timoshenko, S. (1927). Method of analysis of statical and dynamical stresses in rail.

Tvergaard, V., & Needleman, A. (1981). On localized thermal track buckling. International Journal of Mechanical Sciences, 23, 577-587.

Virtanen, P., Gommers, R., Oliphant, T. E., Haberland, M., Reddy, T., Cournapeau, D., . . . Contributors, S. 1. (2020). SciPy 1.0: Fundamental Algorithms for Scientific Computing in Python. Nature Methods, 17, 261–272. doi:10.1038/s41592-019-0686-2

Wilk, S. (2024, March). Lateral Track Strength Increase during Maintenance Speed Restrictions. Tech. rep., MxV Rail. Retrieved from https://www.mxvrail.com/technology-digest/lateral-track-strength-increase-during-maintenance-speed-restrictions/

Wilk, S., Li, D., Gao, Y., & Johnson, C. (2024). FAST Baseline Ballast and Subgrade Characterization. Tech. rep., MxV Rail.

Yang, G., & Bradford, M. A. (2016). Thermal-induced buckling and postbuckling analysis of continuous railway tracks. International Journal of Solids and Structures, 97, 637-649.